International Journal of Latest Engineering and Management Research (IJLEMR)
ISSN: 2455-4847
www.ijlemr.com || REETA-2K16 ǁ PP. 90-116

Analysis and Implementation of an Improved Flyback Inverter for Photovoltaic AC Module Applications

NandarapuUdayaSankaraRedy, Sri.A.Hema Sekhar, Assoc. Professor, EEE

Abstract: Flyback inverter has the advantages such as compactconformation, simple control loop, electric isolation, high step-up ratio, high efficiency, etc., therefore is an attractive solution for photovoltaic ac module applications. In this topology, BCM is more preferred compared to DCM and CCM, because of its higher power level, higher efficiency and wider switching frequency bandwidth. However, the control of BCM is more complicated due to its vari-able switching frequency. This also leads to the difficulty to get the accurate mathematical model between the output current i_{out} and the reference current i_{ref}, which has a great influence on the THD

This paper analyzes and proposes a mathematical model between i_{out} and i_{ref} in BCM through theoretical derivation, and proposes a novel control strategy to generate the reference current that can decrease THD of output current. Meanwhile the realiza-tion of MPPT based on the mathematical model is also investigated. Finally, simulation and experiment results based on an improved flyback-inverter prototype are presented, which validates the pro-posed mathematical model and the control strategy.

Index Terms: AC module, energy conversion, photovoltaicpower systems, system analysis and design.

NOMENCLATURE

ACM: Photovoltaic ac module.
BCM: Boundary conduction mode.
Input capacitance of ACM. Filter capacitance.
: Equivalent capacitance across the MOSFET.
CCM: Continues conduction mode.
DCM: Discontinues conduction mode.
f_o: Frequency of grid voltage.
f_s: Switching frequency.
I_A: Amplitude of i_{out}.
i_c: Input capacitance current.
: Output current of interleaved flyback converter. Current of PV panel.
I_{in}: RMS value of i_{in}.
i_{out}: Output current of PV ACM.
: RMS value of i_{out}.
Primary current of transformer. Peak value of i_p.

i_{ref}: Reference current.
i_s: Secondary current of transformer.
I_s: Peak value of i_s.
L_f: Filter inductance.
L_p: Primary inductance of transformer.
L_s: Secondary inductance of transformer.
L_{ep}: Leakage inductance of L_p.
L_{es}: Leakage inductance of L_s.
L_{mp}: Magnetizing inductance of L_p.
L_{ms}: Magnetizing inductance of L_s.
n: Turns-ratio of transformer.
p_{dc}: Instantaneous input power of PV panel.
P_{in}: Average input power of ACM.
P_{out}: Average output power of ACM.
P_R: Rated output power.
PV: Photovoltaic.
THD: Total harmonic distortion.
T_{on}: Turn-on time of switching cycle.

T_{off}: Turn-off time of switching cycle.
u_{dc}: Voltage of PV panel.
u_{ds}: Drain–source voltage of MOSFET.
u_q: Grid voltage.
V_q: RMS value of u_q .
V_p: Amplitude of u_q .
ZCS: Zero-current switching.

I. INTRODUCTION

HOTOVOLTAIC ac module (PV ACM), also named as P micro-inverter [1], is a compact and modular structure forsmall power PV generation system applications [2]. This con-cept was conceived 30 years ago at Caltech's Jet Propulsion Lab-oratory [3]. However, it is only recently reaching commercial realization. Nowadays, it's recognized as an attractive solution for the residential utility-interactive PV systems [4]–[6].

PV ACM is defined as the integration of a single PV panel and a single-phase grid-tied (GT) inverter [6]. The GT inverter is the direct interface between the PV panel and the residential utility, which converts the low dc voltage from the PV panel to the higher ac voltage of the grid. Compared to the conventional single- or multistring inverters in PV applications, advantages of PV ACM include more flexibility and less installation cost in system expansion as a "plug and play" device, lower manu-facturing cost through mass production, lack of the power mis-match between PV modules, and higher system-level energy harvesting ability under shaded conditions [7].

However, the PV ACM must meet a series of harsh require-ments, such as THD and islanding protection demanded by standards of GT devices, maximum power point track (MPPT) and minimum power fluctuation demanded by PV panels, high efficiency, high reliability, long lifetime, low cost, and easy in-stallation demanded by users [6], [8].

For satisfying these harsh requirements, many topologies and control methods have been reported in references [6], [9], [10]. Nowadays, a single stage flyback-type utility interactive in-verter, which combined a voltage-controlled current-source fly-back and a GT inverter as one single stage [11], is regarded as an attractive solution in PV ACM applications. Its major advantages include electric isolation, high power density, high efficiency, and high step-up ratio, which are based on the sim-ple control loop and compact structure [12]–[14]. But its large input capacity and loss of leakage inductance energy are still the challenges for designers. At present, more and more works have been done on the improvement for the flyback inverter, such as control loop [15]–[21], power decoupling [22]–[25], soft-switching [26]–[28], and MPPT control [29], [30].

In [15]–[20], three operation modes (CCM, DCM, and BCM) of the flyback inverter are investigated in the PV ACM applica-tions. CCM can be realized with average-current control [15]. However, the peak-current control of the secondary current is not appropriate for CCM, since the transformer is incompletely demagnetized during each switching cycle, and the system will behave as a load-independent voltage source with peak-current control [19]. Moreover, the flyback inverter at light load will slip into DCM operation around the zero crossing of grid voltage, which increases the difficulty of control system design [15].

DCM and BCM can be easily realized with peak-current con-trol [17], which has no phase delay compared to the average-current control. Meanwhile, DCM and BCM have the ZCS fea-ture naturally, so can have higher efficiency in comparison with CCM operation. Furthermore, the power density of BCM is usually higher than DCM [19]. Hence, BCM is more preferred for PV ACM applications considering all the earlier research works.

In the BCM with peak-current control, the output current i_{out} is directly controlled by the reference current i_{ref} during each every switching cycle. Since the flyback inverter operates as an ac current source, a variable switching frequency (VSF) control strategy must be applied [17]. However, the VSF f_S leads to the difficulty to get the accurate mathematical model between i_{out} and i_{ref} . As the THD of i_{out} must comply with the standards of GT devices, the mathematical model is extremely important in the design of i_{ref} .

The purpose of this paper is to analyze and propose an ac-curate mathematical model between i_{out} and i_{ref} through theo-retical derivation. Based on the proposed mathematical model, the relationship between f_S and i_{ref} is also analyzed. Then, a novel control strategy of i_{ref} is proposed to decrease THD of Moreover, the realization of MPPT based on this control strategy is also investigated. Finally, the control strategy is ver-ified based on an improved flyback-inverter topology, which is described in [27]. Both simulation and experiment results on this topology are shown in this paper.

This paper is organized as follows. In Section II, the residential utility-interactive PV system and the improved

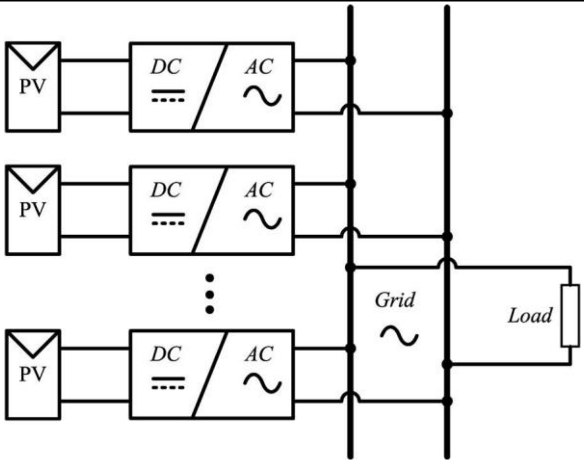

Fig. 1. Residential utility-interactive PV system.

flyback-inverter topology employed in this paper are described. Section III analyzes and proposes the mathematical model be-tween i_{out} and i_{ref} in BCM by theoretical derivation. Section IV proposes the control strategy of i_{ref} and f_s for the improved flyback inverter in BCM operation. Section V analyzes the re-alization of MPPT based on the proposed mathematical model. Simulation and experiment results are then presented in Sections VI and VII, respectively, which validates the performance of the proposed mathematical model. In Section VIII, the conclusions of this paper are given.

II. IMPROVED FLYBACK-INVERTER TOPOLOGY

A. Residential Utility-Interactive PV System

The residential PV system has great potential of being a sig-nificant market, due to following advantages [31], [32]: 1) trans-lating the utility value into an allowable system cost using the homeowner economic parameters and 2) the PV system is able to utilize the roof for support structure, eliminating the land and direct structure expenses.

Fig. 1 shows the diagram of the residential utility-interactive PV system based on ACM device [4], [5]. In this system, the PV array is mounted on the customer's roof, the consumer's load is connected at the ac line terminal, and the ACM can be mounted on each individual PV panel as a modular device [22]. The available dc power from the PV panel varies with the solar irradiation and ambient temperature [33], is converted to the single-phase 50/60 Hz ac power and fed to the utility line through ACM. In the daytime, the solar power supplies to the consumer and the surplus is fed to the utility line, while in cloudy weather or after dusk, the utility line feeds the load.

B. Flyback Inverter

Fig. 2 shows the topology of the flyback inverter, which con-sists of three MOSFETs, two diodes, and a flyback transformer with center-tapped secondary winding. The two outputs from the transformer are connected to the grid, through a common filter circuit, which can switch reciprocally and synchronously with the polarity of the grid voltage. Hence, the flyback-inverter

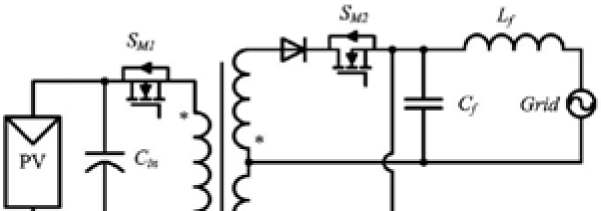

Fig. 2. Fundamental flyback-inverter topology.

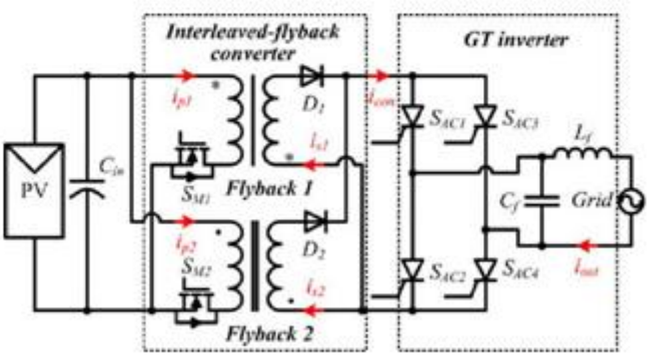

Fig. 3. Improved flyback-inverter topology.

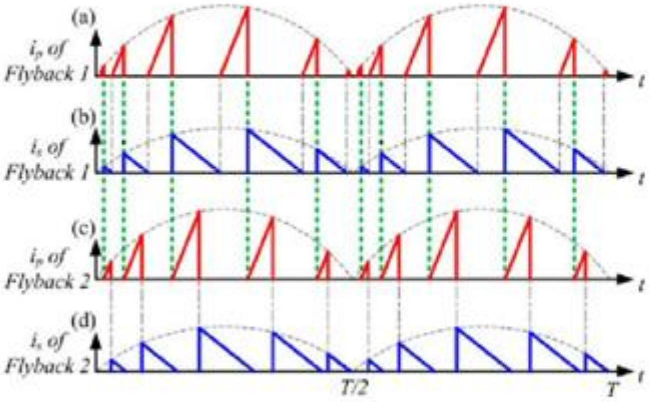

Fig. 4. Principle of interleaved-flyback converter

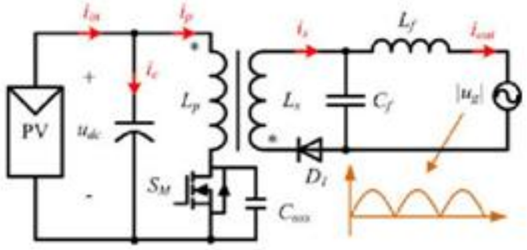

Fig. 5. Equivalent diagram of a single flyback inverter

III. MATHEMATICAL MODEL OF THE BCM OPERATING FLYBACK INVERTER

This section analyzes and proposes the mathematical model between i_{out} and i_{ref} in a BCM operating flyback inverter. Be-cause the operation of the improved topology is the same as the fundamental topology, the following analysis is mainly based on the fundamental flyback inverter for simplification.

A. BCM Operation

Due to the polarity switching circuit, the operations of the flyback inverter are the same during both the positive and neg-ative half cycle of the grid voltage. Therefore, the equivalent diagram for a single flyback inverter can be shown as Fig. 5. According to this figure, the output current i_{out} is obtained by filtering secondary current i_s .

In BCM operation, the peak value I_p of the primary current $i_p$is forced to follow the reference current i_{ref}. During eachswitching cycle, when i_s decreases to zero, S_M conducts, and this process can be realized by quasi-resonant (QR) control. When S_M switches on, i_p increases gradually in a linear relation with u_{dc} . Once i_p equals to i_{ref}, S_M is off and i_s decreases linearly with u_g . Therefore, the relationship between i_{out} and in BCM during half one cycle is shown in Fig. 6. In this figure, the envelope of i_p equals to i_{ref} and i_{out} can be regarded as the average current of i_s during each switching cycle.

According to Fig. 6, the switching frequency varies with i_{ref} in BCM operation, which is more complicated than in DCM operation. The VSF f_s leads to the difficulty to get the accurate mathematical model between i_{out} and i_{ref}. Meanwhile, due to the requirements of the GT devices, i_{out} should be a perfect sinusoidal waveform, while have the same frequency and phase with the utility. That means the accurate mathematical model is extremely important.

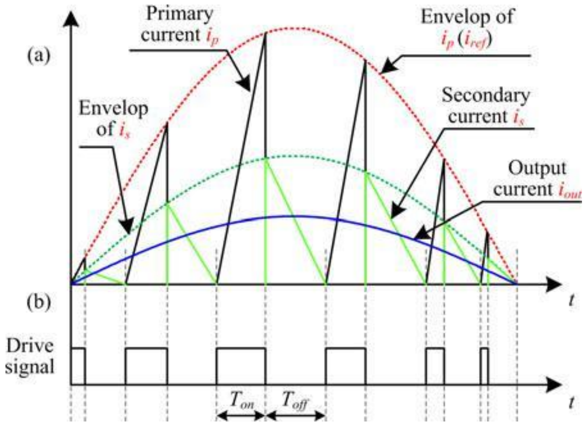

Fig. 6. Relationship between i_{out} and i_{ref} in BCM.

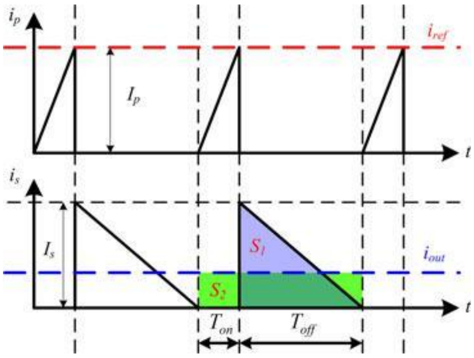

Fig. 7. Primary and secondary currents

B. Proposed Mathematical Model Between i_{out} and i_{ref}

The proposed mathematical model between i_{out} and i_{ref} in BCM operation will be analyzed through theoretical derivation with two fundamental assumptions as:

1) since the flyback inverter operates at high switching fre-quency, u_{dc}, u_g, and i_{ref} can be assumed as constants during each switching cycle;
2) all the components in the circuit are ideal, therefore the leakage inductance of transformer, switching loss and other parasitic parameters of the circuit (such as C_{oss}) are not taken into account.

Fig. 7 shows the primary and secondary currents in the switch-ing cycles. According to the volt-second balance of inductance, the turn-on and turn-off times can be expressed as (1). And the relationship of I_p and I_s can be shown as (2)

$$T_{on} = Lp \cdot Ip \cdot ud\ \frac{1}{c}\ 1 \qquad (1)$$

$T_{off} =$

—

$Ls \cdot Is \cdot ug$

$$I_p = i_{ref}$$

$$I_s = n \cdot I_p = I_p \quad \frac{\overline{L_s}}{L_s} \cdot \qquad (2)$$

Since i_{out} is obtained by filtering the secondary current i_s ,i_{out}approximately equals to the average value of $i_s$dur-ing each switching cycle. So, the area S_1 and S_2 can be thought as equal, as shown in Fig. 7. Therefore, i_{out} can be expressed as (3)

$$i_{out} = \frac{1}{T_{on}+T_o} \cdot \frac{1}{2} \cdot I_s \cdot T_{off} \qquad (3)$$

$$i_{out} = \frac{1}{2} \cdot \frac{i_{ref} \quad L_p/L_s \cdot L_s \cdot i_{ref} \quad L_p/L_s \cdot (1/u_g)}{i_{ref} \cdot L_p \cdot (1/u_{dc}) + L_s \cdot i_{ref}} \qquad (4)$$

Substituting (1) and (2) into (3), (4) can be obtained. After simplification, the ideal mathematical model between *i*o u t and *i*re fcan be obtained as (5). This is the proposed mathematicalmodel, which can be applied in the single flyback inverter. Ac-cording to this expression, *i*re f is determined by the grid voltage *ug*, the input voltage *u*d cand the turns ratio *n* of transformer. Inthe PV ACM application, the input voltage is decided by the PV panel and input capacitor *C*in , and there is usually a large input capacitor that is used to obtain steady input voltage. So, *u*d c can be regarded as constant in the steady state. Therefore, the proportion of *i*re f and *i*o u t varies with *ug* in the line-frequency cycle according to the following equation:

$$i_{ref} = 2 i_{out} \left(\frac{u_g}{u_{dc}} + \frac{L_s}{L_p} \right). \qquad (5)$$

C. Analysis of the Output Current's THD

According to the proposed mathematical model, the output current *i*o u t can be controlled by the reference current *i*re f , and *i*re fcan be obtained by substituting the expression of *i*o u tinto (5). Since PV ACM is a GT device, *i*o u t should comply with the THD requirement. If the mathematical model is inaccurate, *i*o u t will be distorted. Therefore, the accurate mathematical model is the key to guarantee the THD of *i*o u t meet the standard require-ments.

References [17]–[19] treated the envelope of peak primary current *ip* as a sinusoidal waveform in BCM operation, which is similar to the expression of *ip* in DCM operation as shown in
(6) [34]

$$i_{ref} = 2 \frac{P_o}{L_p \cdot f_s} \cdot \sin\omega t. \qquad (6)$$

Reference [17] and [19] adopted (7) as the control law of i_{out} . According to these references, $T_{on\cdot p}$ is the T_{on} interval value referring to the switching cycle that occurs at the time area of $\omega t = \pi/2$, and is a constant. The expression of i_{ref}in [18] is notclearly presented, but it is similar to (7), which can be proved by the fifth figure of reference [18]

$$i_{ref} = \frac{u_{dc}}{L_p} T_{on,p} \sin\omega t. \qquad (7)$$

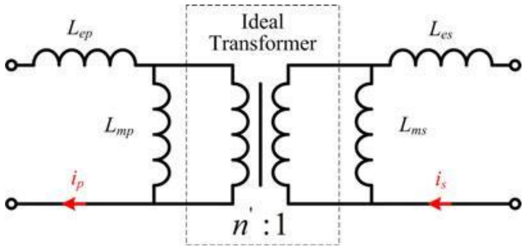

Fig. 8. Modified transformer model.

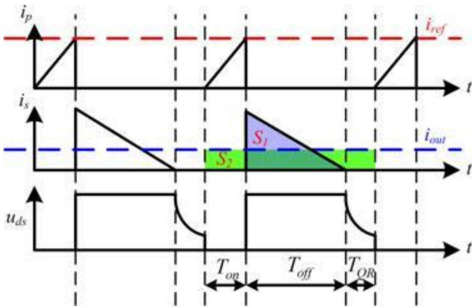

Fig. 9. Waveforms of the QR control.

If these equations are used to calculate the i_{ref} in BCM op-eration, it has little influence on the system efficiency, but i_{out} will be distorted and THD will increase. It is verified by the simulation results in Section VI-C.

D. Further Discussions on the Proposed Mathematical Model

As mentioned earlier, some practical aspects are not consid-ered in the ideal mathematical model. As an instance, the trans-former's leakage inductance is an important factor considering the system power loss [12], while the QR control is a preferred approach for BCM operation to realize soft-switching [20]. Both of them have a measure of influence on the accuracy of the pro-posed mathematical model.

Fig. 8 is a more realistic model of the transformer, which includes the influnce of the leakage inductances. The leakage inductances can be described in (8). Therefore, the relationship of I_p and I_s should be modified as (9)

$$L_p = L_{mp} + L_{ep}$$
$$L_s = L_{ms} + L_{es} \qquad (8)$$

$$I_s = I_p \frac{L_{mp}}{L_{ms}} = I_p \frac{L_p - L_{ep}}{L_s - L_{es}}. \qquad (9)$$

Fig. 9 shows the waveforms of the QR control, and its princi-ple is elaborated in [20]. In this figure, u_{ds} is the drain–source voltage of MOSFET S_M . Compared to the ideal case shown in Fig. 7, there are an additional period designated as the QR time T_{QR}in Fig. 9. Therefore, Equation (3) should be changed intothe following expression:

$$\bar{i}_{out} = \frac{1}{2} \cdot I_s \cdot T_{off} \cdot \frac{1}{T_{on} + T_{off} + T_{QR}}. \qquad (10)$$

According to [20], T_{QR} can be described as (11). C_{oss} is the equivalent capacitance across the MOSFET, as shown in Fig. 5. It is clear as in (11) that T_{QR} is determined by the hardware parameters. Therefore, it can be regarded as a fixed dead-band time in (10). Considering the VSF control technique in BCM operation, T_{QR} should be designed as small as possible

$$T_{QR} = \pi \sqrt{L_p C_{oss}}. \qquad (11)$$

After substituting (1) and (9) into (10), the modified mathematical model can be obtained as (12). However, this is too complicated and hard to be simplified into a linear function as (5), which is fatal to the realization of reference current calcu-lation in practical application

$$i_{out} = \frac{1}{2\pi} \cdot \frac{i_{ref}\cdot(L_p - L_{ep})/(L_s - L_{ms})}{(u_g/i_{ref})\cdot C_{oss}/L_s + (u_g/u_{dc})\cdot L_p/L_s + 1}.$$

(12) Moreover, the leakage inductance and the QR time are not dominant in the system, and they can be minimized through the hardware optimization. Therefore, this paper employs the ideal mathematical model, as shown in (5), in flyback-inverter application after taking all factors as a whole. The performance of the ideal mathematical model is verified by the simulation and experiment results, which are presented in the following sections.

IV. CONTROL STRATEGY FOR THE IMPROVED TOPOLOGY

In this section, the control strategy of the reference current i_{ref} and the switching frequency f_s for the improved topologyin BCM operation is analyzed and designed, which is based on the proposed mathematical model in Section III.

A. Reference Current Analysis

Equation (5) shows the mathematical model between i_{out} and i_{ref}, thus i_{ref} can be obtained by substituting the expression of i_{out} to (5). Because PV ACM is a GT device, i_{out} should comply with the THD requirement, and the ideal condition is to guarantee i_{out} as a perfect sinusoidal waveform. Moreover, i_{out} should have the same frequency and phase with the grid voltage u_g to make sure ACM supply the maximum active power to thegrid. So, i_{out} and u_g can be described as follows:

$$\begin{aligned} i_{out} &= I_A \sin(\omega t) \\ u_g &= V_p \sin(\omega t) \end{aligned} \qquad (13)$$

Substituting (13) into (5), the reference current i_{ref} in BCM for a single flyback inverter can be obtained as follows:

$$i_{ref} = 2I_A\left(\frac{V_p}{u_{dc}}\sin^2(\omega t) + \frac{L_s}{L_p}\sin(\omega t)\right). \qquad (14)$$

In the improved topology, the two flybacks will share the output power of ACM equally when they work in the interleaved mode. Therefore, the reference current of each flyback should

be half of i_{ref}, which can be shown as follows:

$$i_{ref1} = i_{ref2} = I_A\left(\frac{V_p}{u_{dc}}\sin^2(\omega t) + \frac{L_s}{L_p}\sin(\omega t)\right). \qquad (15)$$

B. Switching Frequency Analysis

Since the switching frequency varies with i_{ref} in BCM op-eration, the variation range of f_s should be considered in the flyback-inverter design. As mentioned in Section III-D, the in-fluence of T_{QR} is ignored in the calculation of i_{ref} in order to get a simplified linear mathematical model. This is important for the realization of the reference current calculation in digital control. However, in the analysis of f_s, T_{QR} should be consid-ered to get more precise mathematical model after that i_{ref} has been defined. Therefore, f_s can be described as follows:

$$f_s = \frac{1}{T_{on} + T_{off} + T_{QR}}. \qquad (16)$$

After substituting (1), (2) and (11) into (16), formula (17) can be obtained, which appears that f_s is inversely proportional to i_{ref} when u_g is stable. However, i_{ref} also varies with u_g due to(14), so formula (17) is not yet simplified

$$f_s = \frac{1}{i_{ref}\cdot\left(L_p\cdot\frac{1}{u_{dc}} + L_s\cdot L_p/L_s\cdot(1/u_g)\right) + \pi L_p C_{oss}}.$$

(17) Therefore, the final formula (18) can be obtained by substi-tuting (13) and (14) into (17). Equation (18), as shown at the

bottom of the page.

According to (14) and (18), one conclusion is that i_{ref} is proportional to I_A and f_S can be approximately regarded as inversely proportional to I_A . Moreover, the maximum and min-imum of f_S also can be calculated, as shown in (19). In these equations, u_{dc} is assumed as a constant during each switching cycle

$$f_{s.\max} = \frac{1}{2I_A L_S/V_p + \pi\sqrt{L_p C_{\mathrm{oss}}}}, \qquad t = 0, \frac{\pi}{\omega}$$

$$f_{s.\min} = \frac{1}{2I_A\left(\sqrt{\frac{V_p L_p}{u_{\mathrm{dc}}^2}} + \sqrt{\frac{2L_p L_s}{u_{\mathrm{dc}}}} + \frac{L_s}{V_p}\right) + \pi\sqrt{L_p C_{\mathrm{oss}}}}, \quad t = \frac{\pi}{2\omega} .$$

(19) Due to (15), i_{ref1} and i_{ref2} of the improved topology are both half of i_{ref} , when two flybacks work in the interleaved mode. So, the switching frequency of each phase flyback can be obtained

$$f_S = \frac{1}{2I_A\left(\sqrt{(V_p L_p \sin^2(\omega t)/u_{\mathrm{dc}}^2)} + \sqrt{(2L_p L_S \sin(\omega t)/u_{\mathrm{dc}})} + (L_S/V_p)\right) + \pi\sqrt{L_p C_{\mathrm{oss}}}} \tag{18}$$

$$f_{S1} = f_{S2} = \frac{1}{I_A\left(\sqrt{(V_p L_p \sin^2(\omega t)/u_{\mathrm{dc}}^2)} + \sqrt{(2L_p L_S \sin(\omega t)/u_{\mathrm{dc}})} + (L_S/V_p)\right) + \pi\sqrt{L_p C_{\mathrm{oss}}}} \tag{20}$$

TABLE I
VALUES OF CIRCUIT PARAMETERS

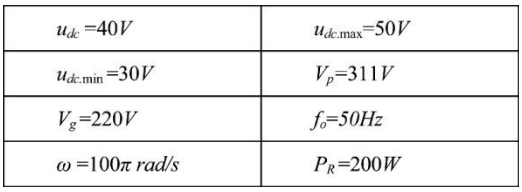

$u_{dc}=40V$	$u_{dc.\max}=50V$
$u_{dc.\min}=30V$	$V_p=311V$
$V_g=220V$	$f_o=50Hz$
$\omega=100\pi\ rad/s$	$P_R=200W$

by substituting (13) and (15) into (17), shown as (20), at the bottom of the page

C. Parameters Design

A 200 W PV ACM prototype at 220 V/50 Hz utility condition is designed in this paper. Table I lists the values of the circuit parameters in the improved topology. The PV panel voltage u_{dc} is 40 V when PV panel outputs the maximum power, while its acceptable input range is 30 V-50 V in the design.

The value of I_A is related to P_{out} , shown as (21). When P_{out} equals to the rated power P_R (200 W), I_A is 1.286 A. I_A will be adjusted by MPPT control method to track the maximum power point, which will be shown in Section V

$$I_A = \frac{2P_{\mathrm{out}}}{V_p} . \tag{21}$$

The relationship of P_{out} and P_{in} is shown in (22). The max-imum output power P_{out} of ACM is 200 W, and the required efficiency η is above 90% when P_{out} is 200 W. So, P_{in} should be less than 222 W at full load

$$P_{\mathrm{out}} = P_{\mathrm{in}} \cdot \eta. \tag{22}$$

The switching frequency variation range of the transformer for each phase flyback is chosen at first. Because of the vol-ume and weight requirements, the optimal range is between 300–400 kHz. Meanwhile the minimum should be more than 200 kHz, and the maximum should be less than 600 kHz.

1) Transformer Design: In the improved topology, the inter-leaved flyback comprises two current-source flybacks. So, the turns ratio n should be determined by the inverse ratio of the in-put current and output current, which can be calculated by (23). In this equation, I_{in} and I_{out} are the root-mean-square (rms) value of i_{in} and i_{out} , respectively

$$I_{in} = \frac{P_{in}}{u_{dc}} \qquad I_{out} = \frac{P_{out}}{V_g} \quad . \qquad (23)$$

Therefore, the turns ratio n is designed according to (24). The required value is 1:6.11 when u_{dc} is 40 V, 1:4.44 when u_{dc} is

50 V, and 1:8.15 when u_{dc} is 30 V,
respectively. Finally, n is selected as 1:6

$$n = \frac{I_{out}}{I_{in}} = \frac{\eta \cdot u_{dc}}{V_g} \quad . \qquad (24)$$

In the improved topology, the reference current of each fly- back should be half of i_{ref} , shown as (15), when the two flybacks work in the interleaved mode. This equation can be rewritten as (25), and the maximum primary current $I_{p.max}$ can be calculated shown as (26)

$$i_{ref1} = i_{ref2} = I_A \frac{V_p}{u_{dc}} \sin^2(\omega t) + \frac{1}{n} \sin(\omega t) \qquad (25)$$

$$I_{p.max} = I_A \frac{V_p}{u_{dc}} + \frac{1}{n} , \quad t = \frac{\pi}{2\omega} . \qquad (26)$$

Then, the primary inductance L_p can be obtained from (27) according to reference [35]. In the equation, δ_{max} is the max-imum duty cycle, which is usually 0.5 in the design of the traditional flyback converter. According to (19), when i_p equals to $I_{p.max}$, the switching frequency f_s is the minimum, which is 200 kHz

$$L_p = \frac{u_{dc.min} \cdot \delta_{max}}{I_{p.max} \cdot f_s} \quad . \qquad (27)$$

Therefore, the required L_p is 3.564 μH. Then, the secondary inductance L_s can be calculated by (28), which is 128.3 μH. Subsequently, the primary and secondary inductances are ad-justed according to the experiment results, and finally the mea-sured value is 3.7 and 133.6 μH, respectively

$$L_s = \frac{L_p}{n^2} \quad . \qquad (28)$$

2) Input Capacitance Design: This topology needs a verylarge dc input capacitance C_{in} to decouple the power pulsation caused by single-phase power generation to the utility line [22]. The value of C_{in} can be calculated according to (29) in [34]. In this formula, u_{dc} is 2 V. So, the required capacitance is 8.83 mF. In this paper, C_{in} is comprised of four 2.2 mF electrolytic capacitors in parallel

$$C_{in} = \frac{P_{in}}{\omega u_{dc} u_{dc}} \quad . \qquad (29)$$

However, the electrolytic capacitor with large capacitance has a large volume and a relatively short lifespan. Especially under a very high atmospheric temperature, the lifetime of the electrolytic capacitor is shortened dramatically [22]. In order to solve this problem, some power decoupling circuits and control methods are proposed in [22]–[25]. In these references, the power decoupling capacitance is about 20–50 μF, which can be replaced by the film capacitors. And this will be the future work of this topology.

3) Output Filter Design: Fig. 10 shows the equivalent dia-gram of CL filter in the topology, and the relationship of i_s, i_{out} and u_g can be shown as (30). Thus, the expression of the CL filter can be obtained as shown in (31)

$$I_{out}(s) = \frac{1}{1+s^2L_fC_f} I_s(s) - \frac{sC_f}{1+s^2L_fC_f} U_g(s) \quad (30)$$

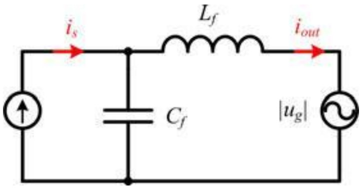

Fig. 10. **Equivalent diagram of CL filter.**

TABLE II
DESIGNED VALUES OF CIRCUIT PARAMETERS

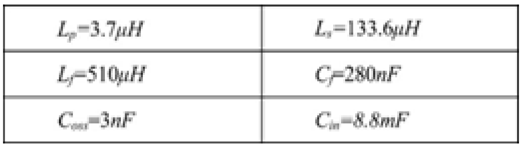

L_p=3.7μH	L_s=133.6μH
L_f=510μH	C_f=280nF
C_{oss}=3nF	C_{in}=8.8mF

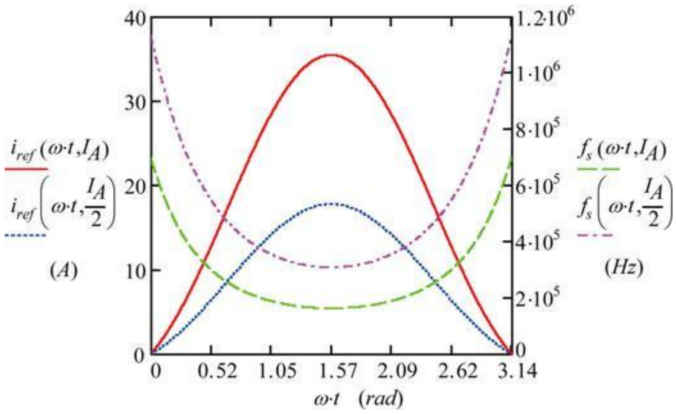

Fig. 11. i_{ref} and f_s of single flyback inverter.

$$\left.\frac{I_{out}(s)}{I_s(s)}\right|_{U_g(s)=0} = \frac{1}{1+s^2L_fC_f}$$
$$\left.\frac{I_{out}(s)}{U_g(s)}\right|_{I_s(s)=0} = \frac{sC_f}{1+s^2L_fC_f} \quad (31)$$

This is a second-order low-pass filter with a resonant fre-quency f_r , which can be expressed as (32). In this design, f_r should comply with (33) [20]. Therefore, the range is from 500 Hz to 20 kHz. Finally, L_f and C_f are selected as 510 μH and 280 nF, respectively, considering the requirement of volume and cost. And the resonance frequency is 13.3 kHz

$$f_r = \frac{1}{2\pi\sqrt{L_fC_f}} \quad (32)$$

$$10f_o \leq \frac{1}{2\pi\sqrt{L_fC_f}} \leq \frac{1}{10} f_{s.min} \quad (33)$$

D. Design of the Reference Current for Improved Topology

Table II lists the designed values of circuit parameters. Ac-cording to the values of Tables I and II, i_{ref} and f_s of single flyback inverter can be shown as in Fig. 11. In this figure, $i_{ref}(\omega t, I_A)$ is the reference current for single flyback inverter, and $f_s(\omega t, I_A)$ is its switching frequency, $i_{ref}(\omega t, I_A/2)$ is the reference current for each flyback converter in the interleaved mode, and $f_s(\omega t, I_A/2)$ is its switching frequency.

This figure illustrates that i_{ref} is very small at the zero cross-ing, which causes f_s extremely high at this time. However, the acceptable range of f_s is expected as 200–600 kHz. Therefore, the principle of the improved topology is designed as follows to comply with the requirement, which is also used in refer-ence [27], [34]:

1) when i_{ref} is smaller than a value defined as I_1, both two flybacks stop working. This period can be called as dead band;
2) when i_{ref} is larger than I_1 and smaller than I_2, the first flyback works in stand-alone mode;

when i_{ref} is larger than I_2, both two flybacks work in the interleaved mode

$$I_1 = i_{ref}(\omega t_1) \qquad I_2 = i_{ref}(\omega t_2) \tag{34}$$

The expression of I_1 and I_2 can be described as (34). There-fore, i_{ref1} and i_{ref2} of the two flyback are designed as (35) and (36). Then, f_{s1} and f_{s2} of two flyback can be expressed as (39) and (40), as shown at the bottom of the next page, which are corresponding to (35) and (36)

$$i_{ref1}(\omega t) = \begin{cases} 0 & (0 \le i_{ref}(\omega t) < I_1) \\ i_{ref}(\omega t) & (I_1 \le i_{ref}(\omega t) < I_2) \\ i_{ref}(\omega t)/2 & (I_2 \le i_{ref}(\omega t)) \end{cases} \tag{35}$$

$$i_{ref2}(\omega t) = \begin{cases} 0 & (0 \le i_{ref}(\omega t) < I_2) \\ i_{ref}(\omega t)/2 & (I_2 \le i_{ref}(\omega t)) \end{cases} . \tag{36}$$

The value of I_1 is related to the dead band time and $f_{s.max}$. The larger the I_1 is, the smaller the $f_{s.max}$ is. But if I_1 is too large, the dead band time will be increase, which will also increase the THD of i_{out}. Therefore, the value of I_1 should be carefully selected to guarantee that $f_{s.max}$ complies with the design requirement and the dead band time is the minimum. According to equation (18) and (19), $f_{s.max}$ can be expressed as (37) shown at the bottom of the next page.

Therefore, the value of t_1 can be obtained by solving equation (37), and the value of I_1 can be obtained by (34). According to the values in Tables I and II, ωt_1 is 0.077 rad when $f_{s.max}$ is 600 kHz, and the required value of I_1 is 1.306 A.

The selection of I_2 is different from that of I_1 because the variation of I_2 won't cause a dramatic change of $f_{s\cdot min}$. Mean-while, its influence on the THD of i_{out} is weak. Thus its allow-able range is not so limited. Moreover, the time of interleaved mode is controlled by I_2. If P_{out} is small and the peak of i_{ref} is smaller than I_2, the interleaved mode will be disabled, and only one flyback works during the whole period. In this design, the boundary is selected as half of the rated output power, which is 100 W. Therefore, I_2 can be obtained by (38). In this equation, $I_A$is 1.286 A. So, the required value of $I_2$is 17.729 A, which

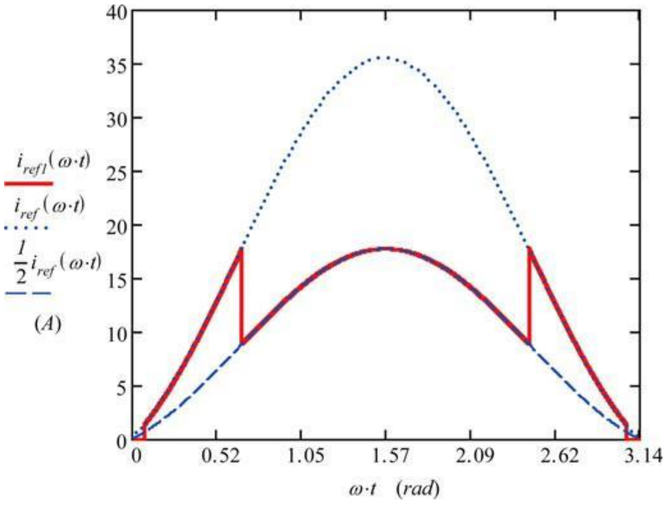

Fig. 12. Reference current of flyback 1

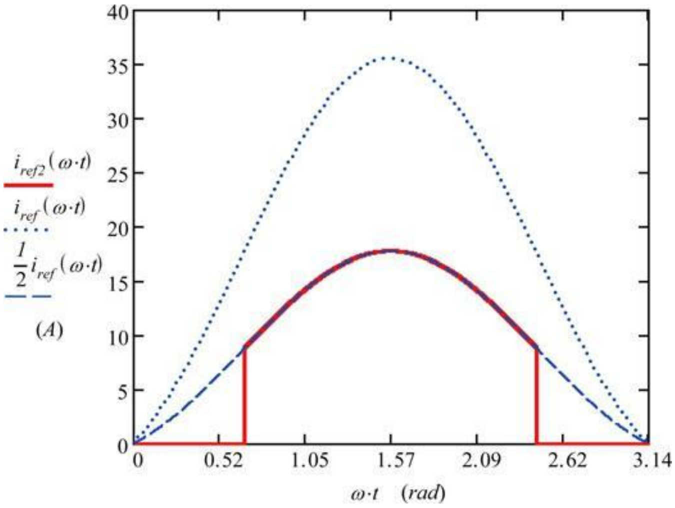

Fig. 13. Reference current of flyback 2.

is half of peak primary current, and ωt_2 is 0.683 rad

$$I_2 = i_{ref}\frac{\pi}{2} = I_A \frac{V_p}{u_{dc}} + \frac{L_s}{L_p}. \qquad (38)$$

After substituting the values of parameters in Table II, i_{ref1}, i_{ref2}, f_{s1}, and f_{s2} can be shown as Figs. 12–14, respec-tively. In these figures, f_s is limited in between 250 and 600 kHz. Meanwhile, when I_1 and I_2 use different values, the influence on THD is shown in Section VI-D

V. REALIZATION OF MPPT CONTROL IN THE IMPROVED TOPOLOGY

Most of the traditional MPPT control methods are applied to the voltage-source converter, and are usually implemented by adjusting input voltage u_{dc} [36]–[40]. However, PV ACM is a current-source system, and input voltage can't be directly controlled, which depends on PV panel characteristics. So, these MPPT methods should be modified and realized by adjusting input current i_{in} to apply to the PV ACM application.

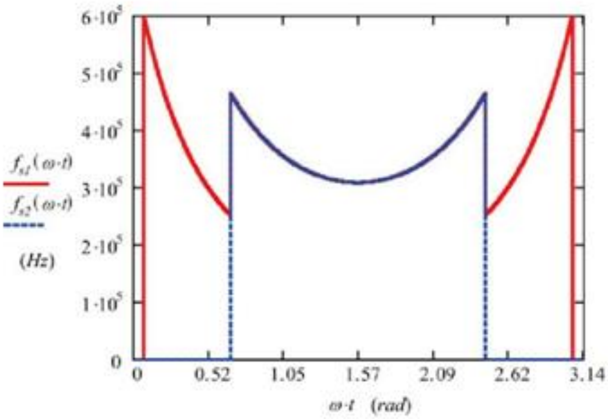

Fig. 14. Switching frequencies of two flybacks

In the flyback inverter, the reference current i_{ref} is used to control the output current i_{out} directly. If the input voltage and grid voltage is stable in line-frequency cycle, the input current i_{in} can be directly controlled by i_{ref}. And the relationship of i_{ref} and i_{in} will be investigated as follows.

According to Fig. 5, the input current i_{in} is the sum of i_p and i_c, so the input power P_{in} can be described as follows:

$$P_{in} = \int_0^T u_{dc}\, i_{in}\, dt = \int_0^T u_{dc}\, i_c\, dt + \int_0^T u_{dc}\, i_p\, dt. \qquad (41)$$

Because u_{dc} is also the voltage across the input capacitor, the relationship of i_c and u_{dc} can be shown in (42). Therefore, (43) can be obtained from (41) and (42)

$$i_c = C\frac{du_{dc}}{dt} \qquad (42)$$

$$P_{in} = \frac{1}{2} C u_{dc}^2 \,{}_0^T + {}_0^T u_{dc} i_P \, dt. \qquad (43)$$

As mentioned earlier, the input voltage u_{dc} can be regarded as a constant in the steady state. So, (41) can be simplified as

shown in (44). Therefore, i_{in} can be regarded as the average of

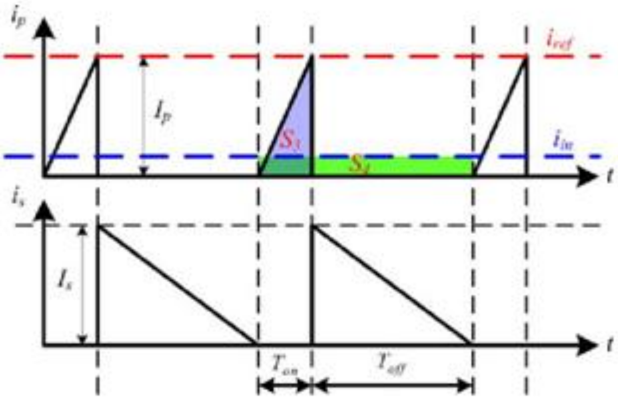

Fig. 15. Primary current and secondary current.

$i_p$during each switching cycle, which is shown in Fig. 15

$$P_{in} = {}_0^T u_{dc} i_P \, dt. \qquad (44)$$

As shown in Fig. 15, i_{in} can be calculated according to the same assumption as i_{out} in the foregoing analysis, which is that the area S_3 (blue) and S_4 (green) are approximately equal. So, the primary current i_{in} can be expressed as (45), which is similar to (3)

$$i_{in} = \frac{1}{2} \cdot I_p \cdot T_{on} \cdot \frac{1}{T_{on} + T_{off}} \qquad (45)$$

After substituting (1) and (2) into (45), (46) can be obtained,

which shows the relationship between i_{in} and i_{ref}. When ACM works at steady state, u_g and u_{dc} can be regarded as stable in line-frequency cycle. Therefore, the input current can be directly

controlled by i_{ref}. This formula also applies to the improved topology, because in the interleaved mode, i_{in} equals to the sum

of two primary currents of each flyback, but their references are half of $i_{\text{re f}}$

$1 \qquad u_g$

$^{i}\text{in} \quad = \quad \cdot\, i_{\text{re f}} \,\cdot \qquad\qquad .$ (46)

1

$^{f}s\,.\,\text{m}$

$\text{a x}^{=}$ (37)

$2I_A \quad (V_pL_p \sin^2(\omega t_1)/u_{\text{d c}}^2) + (2 \qquad L_p\, L_s\sin(\omega t_1)/u_{\text{d c}}) + (L_s/V_p) \;+ \pi \qquad {}^{L}p\ {}^{C}\text{o ss}$

1

V

$p \qquad 2 \qquad 2 \qquad\qquad L_s \qquad\qquad (I_1 \le i_{\text{re f}}(\omega t) < I_2)$

$2I_A \quad u2\ L_p\sin\ (\omega t) + \ \text{c}\ \text{d} \quad {}^{L}p\ {}^{L}s\ {}^{\sin(\omega t)\,+}\,{}_{Vp} \qquad + \pi \quad \breve{}p\ \breve{}\text{o ss}$

d

c

$f_{s1}(\omega t) = \quad 0 \qquad\qquad (0 \le i_{\text{re f}}(\omega t) < I_1)$ (39)

1

$V_p \qquad 2 \qquad 2 \qquad\qquad L_s \qquad\qquad (I_2 \le i_{\text{re f}}(\omega t))$

$I_A \quad u\ L_n\sin\ (\omega t) + \quad \text{d}\ \text{c} \quad L_n\, L_s\sin(\omega t) + V_n \;+ \pi \quad {}^{L}p\ {}^{C}\text{o ss}$

d

c

$0 \qquad\qquad (0 \le i_{\text{re f}}(\omega t) < I_2)$

$f_{s2}(\omega t) = \qquad 1$ (40)

V

$p \qquad 2 \qquad 2 \qquad\qquad L_s \qquad\qquad (I_2 \le i_{\text{re f}}(\omega t))$

$I_A \quad u\ 2\ L_p\sin\ (\omega t) + \ \text{c}\ \text{d} \quad L_p\, L_s\sin(\omega t) + V_n \;+ \pi \quad \breve{}p\ \breve{}\text{o ss}$

d c

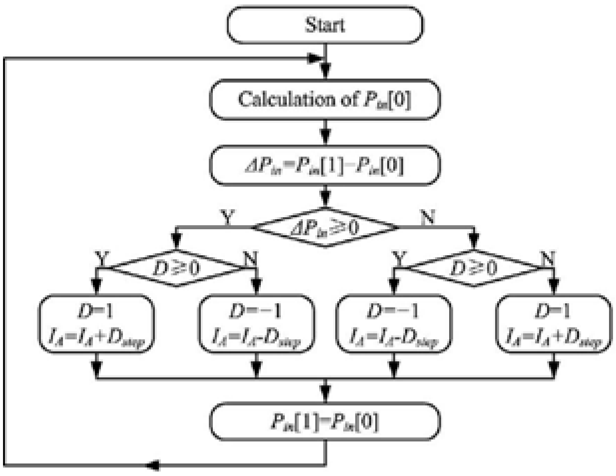

Fig. 16. Diagram of MPPT control

Meanwhile, equation (5) shows that i_{ref} is a function of i_{out}. After substituting (5) into (46), the relationship of i_{in} and i_{out} can be expressed as (47). The equation also proves that, the instantaneous input power $u_{dc} \cdot i_{in}$ equals to instantaneous output power $u_g \cdot i_{out}$ in the ideal state

$$i_{in} = i_{out} \cdot \frac{u_g}{u_{dc}} \qquad (47)$$

$$i_{in} = \frac{V_p}{u_{dc}} \cdot I_A \sin^2(\omega t). \qquad (48)$$

According to the expression of i_{out} and u_g as shown in (13), i_{in} can be obtained as (48), which shows that the input current i_{in} can be adjusted by changing I_A proportionally in the flyback inverter. Therefore, the traditional MPPT methods can be modified and realized by adjusting I_A to apply to the PV ACM application. For example, Fig. 16 shows the conventional "Incremental conductance" algorithm using fixed step-length, which is realized by adjusting I_A. This method is verified by the simulation results in the following section.

VI. SIMULATION RESULTS

A simulation platform based on MATLAB integrated with PLECS is established, in order to verify the mathematical model and the proposed control strategy of BCM operation on the improved flyback-inverter topology. Moreover, MPPT control is implemented by adjusting I_A is also verified. The simulation result is shown as follows.

A. Control Block Diagram of Improved Topology

Fig. 17 shows the control block diagram of simulation plat-form, which is based on the analysis in Section IV. Phase-locked loop (PLL) is used to detect the phase angle, amplitude and fre-quency of grid voltage accurately and quickly. Islanding protec-tion guarantees the ACM works under normal utility condition. The output of MPPT control is I_A ,which is used to adjust the reference current i_{ref}. The whole diagram of Fig. 17 is established in MATLAB. And the power circuit, as shown in Fig. 3, is established in PLECS.

Fig. 17. Control block diagram of ACM.

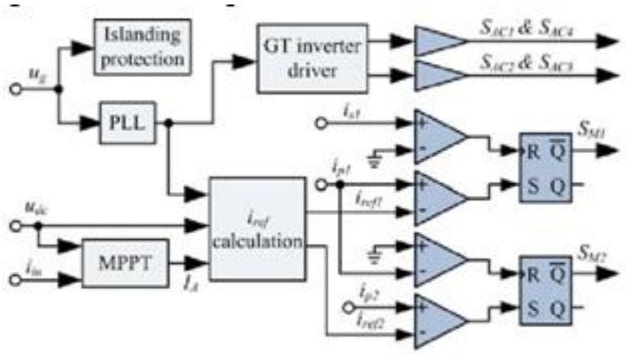

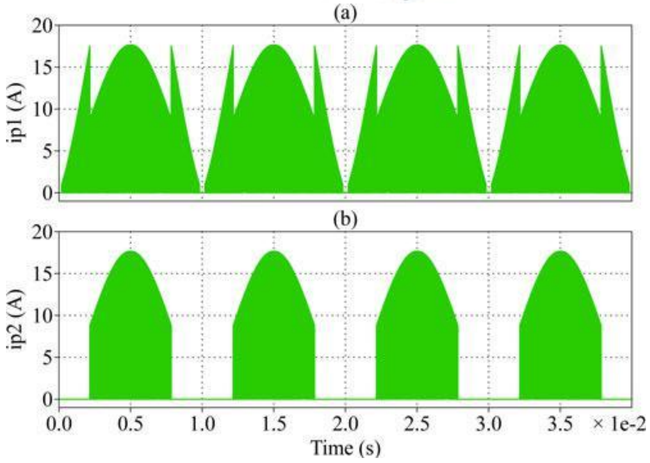

Fig. 18. Primary currents of flyback 1 and 2.

The parameters' value on the simulation platform has been shown in Tables I and II. The amplitude I_A of output current $i_{\mathrm{re\ f}}$is designed as 1.414 A. Only after that simulation resultsmeet the design requirement, the mathematical model and the control strategy can be verified.

B. Simulation Result of Reference Current Design

Fig. 18(a) and (b) illustrates the primary currents i_{p1} and i_{p2} of flyback 1 and 2 in interleaved mode, respectively. The envelopes of primary currents are equal to the reference currents $i_{\mathrm{re\ f1}}$ and $i_{\mathrm{re\ f2}}$, respectively. Fig. 19(a) and (b) shows the secondary currents i_{s1} and i_{s2} of flyback 1 and 2, respectively. Fig. 19(c) shows the output current $i_{\mathrm{c\,o\,n}}$ of the interleaved flyback, which equals to the sum of two secondary currents.

Fig. 20(a) and (b) shows the details of i_{p1} and i_{p2} , respectively. Fig. 21(a) and (b) shows the details of i_{s1} and i_{s2} , respectively. Fig. 21(c) shows the details of $i_{\mathrm{c\,o\,n}}$.

Fig. 22, shows the output current $i_{\mathrm{o\ u\ t}}$ of the improved topol-ogy and the sampling voltage of grid for the comparison of $i_{\mathrm{o\,u\,t}}$ and u_g . The amplitude of $i_{\mathrm{o\,u\,t}}$ meets the design requirements, which is designed as 1.286 A. The THD of $i_{\mathrm{o\,u\,t}}$ is 2.286%, cal-culated by MATLAB. Fig. 23 is the peak magnitude spectrum of

, which proves the harmonic components are in the accepted range.

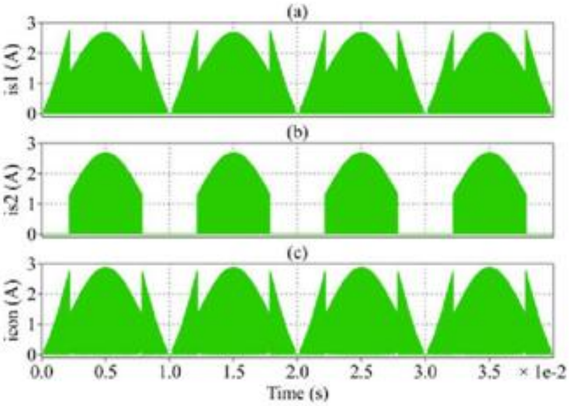

Fig. 19. Secondary currents of flyback 1 and 2.

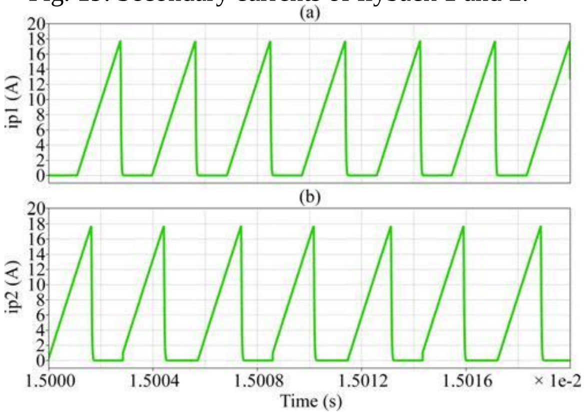

Fig. 20. Details of primary currents.

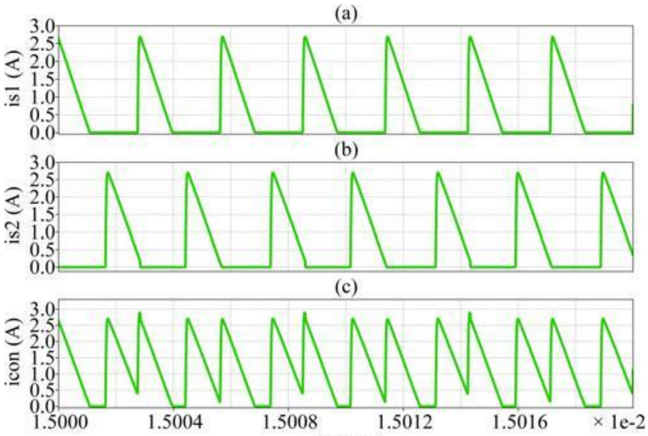

Fig. 21. Details of secondary currents.

C. Comparision With Other Models

According to [17]–[19], the reference current can be ex-pressed as (49). Another reference current is shown as (50) for the comparison. Fig. 24 shows the waveforms of i_{ref}, $i_{ref.a}$ and $i_{ref.b}$. In these equations, the values of A and B equal to the peak

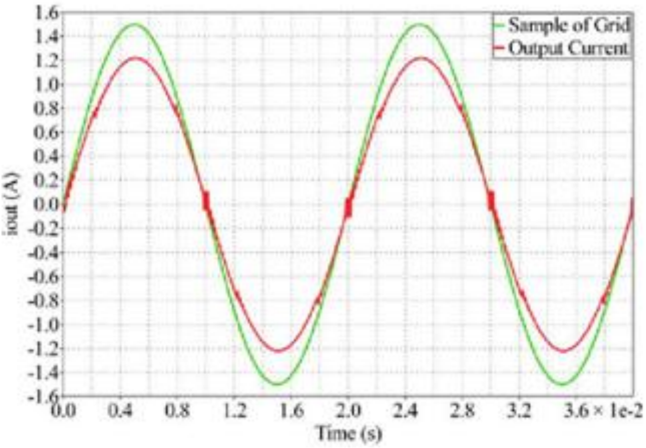

Fig. 22. Output current of ACM and sampling of grid.

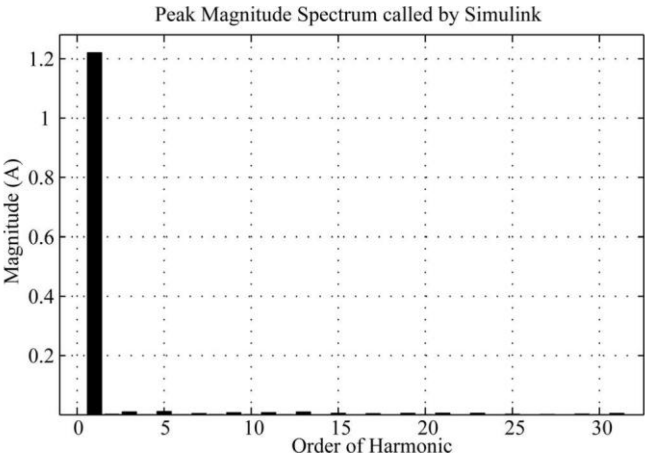

Fig. 23. Spectrum of ACM's output current.

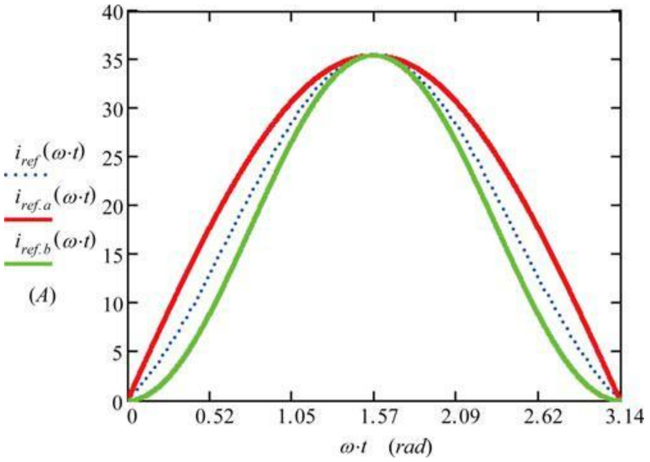

Fig. 24. Waveforms of i_{ref}, $i_{ref.a}$, and $i_{ref.b}$.

primary current (35.458 A), which guarantees the amplitude of i_{out} is close to I_A(1.286 A)

$$i_{ref.a} = A \cdot \sin(\omega t) \qquad (49)$$

$$i_{ref.b} = B \cdot \sin^2(\omega t). \qquad (50)$$

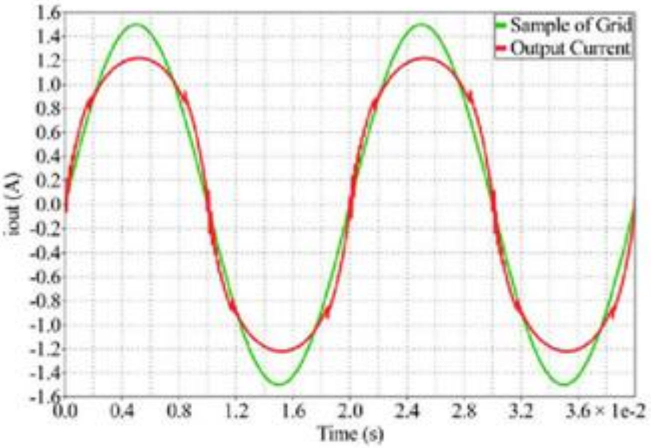

Fig. 25. Output current of ACM using (49).

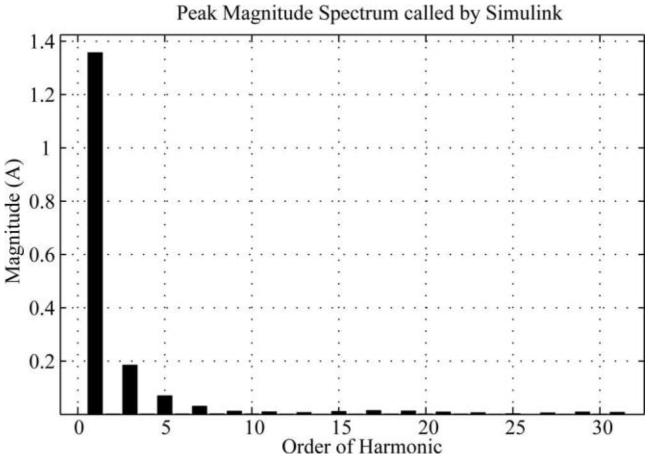

Fig. 26. Spectrum of output current using (49).

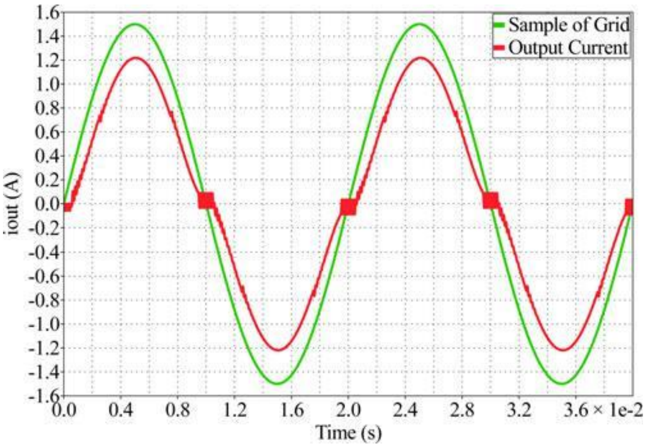

Fig. 27. Output current of ACM using (50).

Fig. 25 shows the output current using (49) as the reference current, Fig. 26 illustrates the spectrum of output current, and the measured THD is 14.84%. Fig. 27 shows the output cur-rent using (50) as the reference current, Fig. 28 illustrates the spectrum of output current, and the measured THD is 13%.

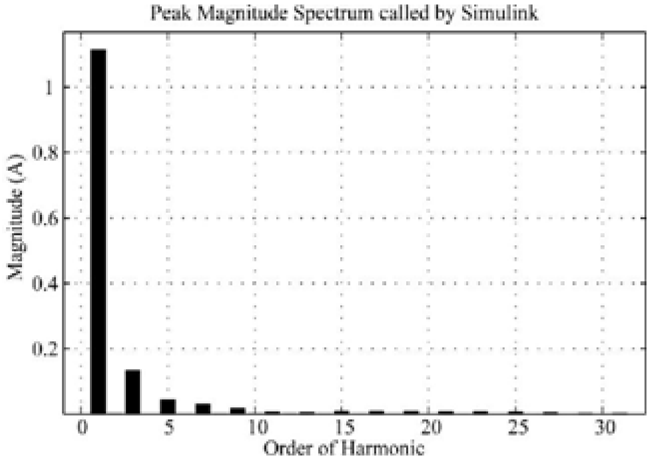

Fig. 28. Spectrum of output current using (50).

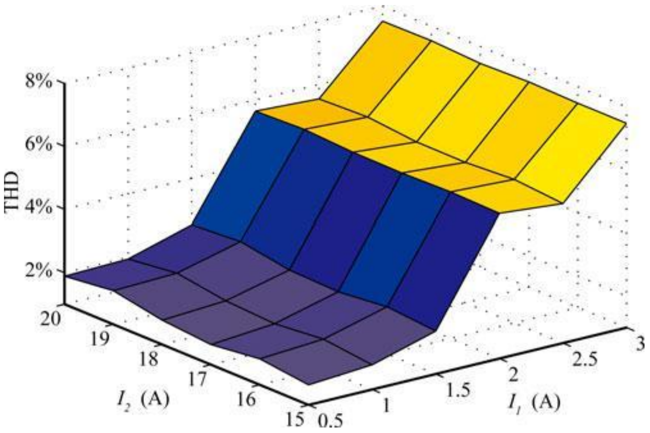

Relationship of I_1, I_2 and THD.

According to the earlier results, when (49) or (50) are adopted as the reference current, THD is much larger than that of the pro-posed mathematical model in this paper. Therefore, the accuracy of the proposed mathematical model is verified.

D. Simulation Result for I_1 andI_2

According to Section IV-D, the values of I_1 and I_2 will affect the THD of i_{out} . Fig. 29 shows the relationship of I_1, I_2 and THD. According to this figure, the increase of I_1 will cause THD deteriorate dramatically. Thus, the value of I_1 should be the min-imum when $f_{s.max}$ complies with the requirement. Meanwhile, the influence on THD is weak when I_2 varies in a large range. Therefore, the allowable range of I_2 is wide.

E. Simulation Result of MPPT Control

Fig. 30 shows the *V–I* curve of PV panel, of which the max-imum power is set as 200 W. Fig. 31 illustrates the simulation result of MPPT control. The steady state starts form 0.18 s, and MPPT control is enabled in 0.24 s. Fig. 31(a) shows the value of I_A, Fig. 31(b) and (c) shows the output voltage $u_{dc}$and current $i_{in}$of PV panel, respectively, and Fig. 31(d) show the aver-age output power of PV panel. From Fig. 31, the conventional

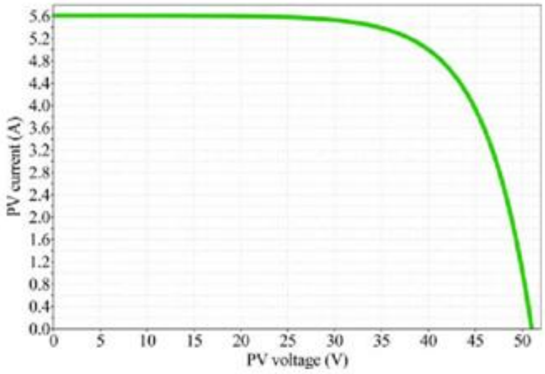

Fig. 30. *V–I* curve of PV panel.

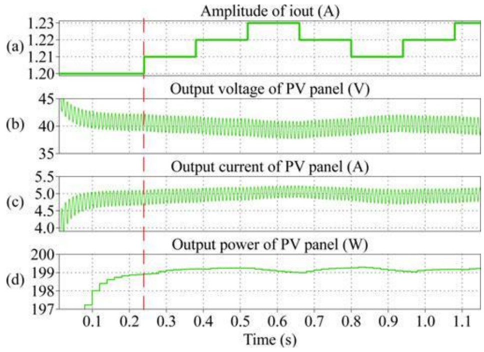

Fig. 31. Simulation result of MPPT control.

“Incremental conductance” algorithm using fixed step-length is realized by adjusting I_A .

VII. EXPERIMENT RESULTS

A 200 W PV ACM prototype at 220 V/50 Hz utility condition was implemented to validate the proposed mathematical model and the control strategy. The control algorithm is the same as Fig. 17, in which the light-color blocks are implemented on the FPGA EP3C10E144 from ALTERA and the dark-color ones are implemented by hardware. The power circuit is still the im-proved flyback-inverter topology. Then, the experimental results are shown as follows.

A. Experiment Result of Reference Current Design

In the experiment, the input voltage of ACM is 36 V, which is supplied by a dc voltage source. The amplitude I_A of output current is designed as 1 A, so the output power should be around 156 W. The values of other parameters are same as Tables I and II.

Fig. 32 shows the primary currents i_{p1} and i_{p2} of flyback 1 and 2 in the interleaved flyback. These currents are measured by two current transformers, respectively, of which the ratio is

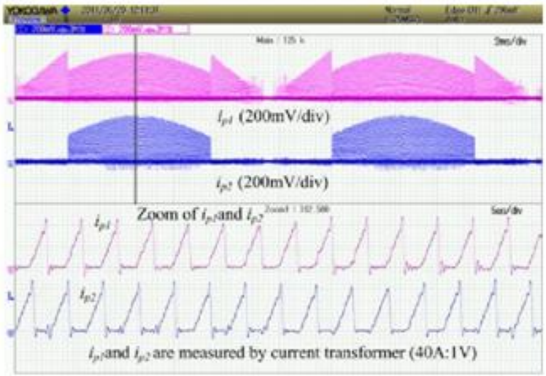

Fig. 32. Primary currents of flyback 1 and 2.

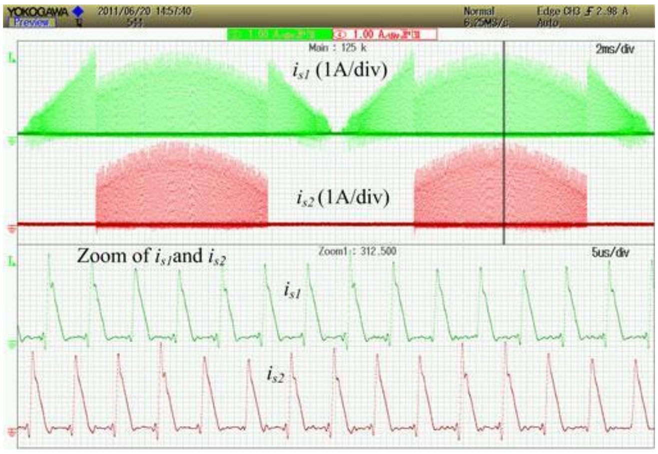

Fig. 33. Secondary currents of flyback 1 and 2.

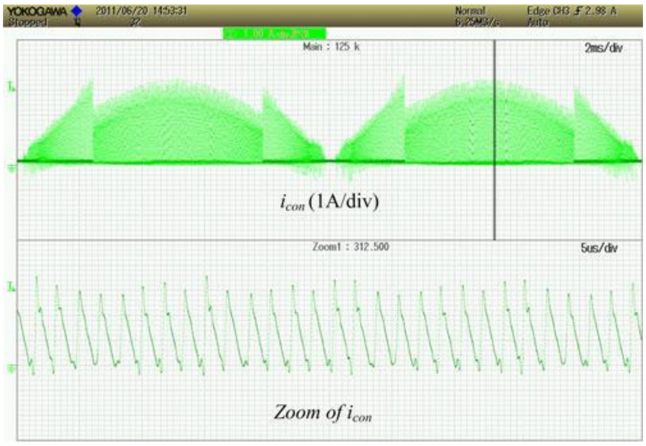

Fig. 34. Output current of interleaved flyback.

40 A:1 V. The envelopes of primary currents are equal to the reference currents. Fig. 33 shows the secondary currents i_{S1} and $i_{s2}$of flyback 1 and 2, measured by the current probe. Fig. 34shows the output current i_{con} of the interleaved flyback, which is equal to the sum of i_{s1} and i_{s2} .

Fig. 35 shows the output current i_{out} of PV ACM and the grid voltage u_g . The output current is a good sinusoidal waveform, but has a little distortion at zero crossing. That is because both

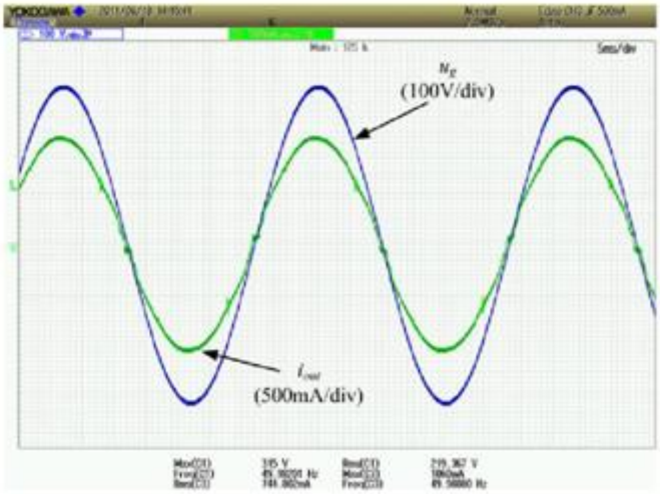

Fig. 35. Output current of ACM and grid voltage.

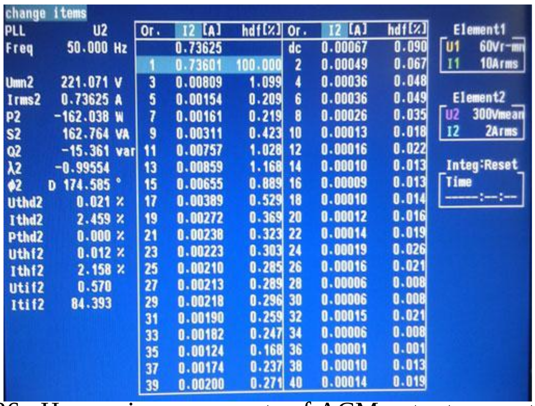

```
change items
PLL          U2       Or.   I2 [A]   hdf[%]  Or.   I2 [A]   hdf[%]     Element1
Freq     50.000 Hz         0.73625           dc   0.00067   0.090     U1   60Vr-mn
                       1   0.73601  100.000   2   0.00049   0.067     I1   10Arms
Umn2    221.071 V      3   0.00809    1.099   4   0.00036   0.048
Irms2   0.73625 A      5   0.00154    0.209   6   0.00036   0.049      Element2
P2     -162.038 W      7   0.00161    0.219   8   0.00026   0.035     U2  300Vmean
S2      162.764 VA     9   0.00311    0.423  10   0.00013   0.018     I2     2Arms
Q2      -15.361 var   11   0.00757    1.028  12   0.00016   0.022
λ2     -0.99554       13   0.00859    1.168  14   0.00010   0.013     Integ:Reset
Φ2    D 174.585 °     15   0.00655    0.889  16   0.00009   0.013     Time
Uthd2     0.021 %     17   0.00389    0.529  18   0.00010   0.014     ------:--:--
Ithd2     2.459 %     19   0.00272    0.369  20   0.00012   0.016
Pthd2     0.000 %     21   0.00238    0.323  22   0.00014   0.019
Uthf2     0.012 %     23   0.00223    0.303  24   0.00019   0.026
Ithf2     2.158 %     25   0.00210    0.285  26   0.00016   0.021
Utif2     0.570       27   0.00213    0.289  28   0.00006   0.008
Itif2    84.393       29   0.00218    0.296  30   0.00006   0.008
                      31   0.00190    0.259  32   0.00015   0.021
                      33   0.00182    0.247  34   0.00006   0.008
                      35   0.00124    0.168  36   0.00001   0.001
                      37   0.00174    0.237  38   0.00010   0.013
                      39   0.00200    0.271  40   0.00014   0.019
```

Fig. 36. Harmonic components of ACM output current.

of the two flybacks do not work in this period and the current is discontinuous. Moreover, the amplitude of current is 1.06 A, which is close to the theoretical value 1 A.

Fig. 36 shows experimental data about the harmonic compo-nents of i_{out}, measured by WT3000 of Yokogawa. Fig. 37 shows the percentage spectrum of i_{out}, which is based on the data of Fig. 36. From these figures, there are some high-frequency har-monics (3rd, 11th, 13th, and 15th) in output current, but their magnitudes are very small. And the THD of i_{out} is 2.459% shown by Fig. 36, which can also prove the good quality of the output current.

According to the experiment results, the proposed mathemat-ical model of BCM operation is validated. Using the proposed control strategy in the experiment, the output current of ACM exhibits good sinusoidal waveform and is very close to the the-oretical value. Moreover, THD and harmonics of i_{out} are in the satisfying range, which meet IEC61727 [41] and IEEE1547 [42] standards quite well, verifying the excellent performance of the control strategy.

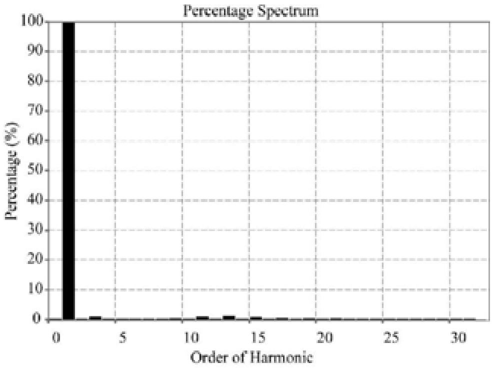

Fig. 37. Percentage spectrum of harmonics.

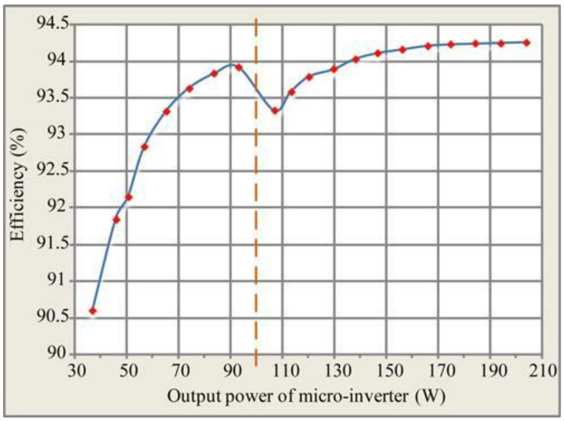

Measured efficiency versus output power of ACM.

B. Experiment Result of Efficiency

In this experiment, the input voltage of ACM is 36 V, which is supplied by a dc voltage source. Fig. 38 shows the measured efficiency versus output power of the ACM, which is measured by WT230 of Yokogawa. When the load is between 60 and 140 W, the efficiency is above 93%, and when the load is between 140 and 200 W the efficiency is above 94%. The experiment result shows the proposed control strategy in BCM operation guarantees high efficiency at different load condition.

Moreover, according to the principle of interleaved flyback, only one flyback converter of the ACM works when P_{out} is less than 100 W, and two flyback converters of the ACM work in the interleaved mode when P_{out} is more than 100 W. Since the output power is shared equally by the two flybacks in the interleaved mode, the efficiency between 100 and 130 W is smaller than that between 70 and 100 W.

C. Experiment Result of MPPT Control

In this experiment, the input power of ACM is supplied by a PV panel, of which the maximum power is around 140 W.

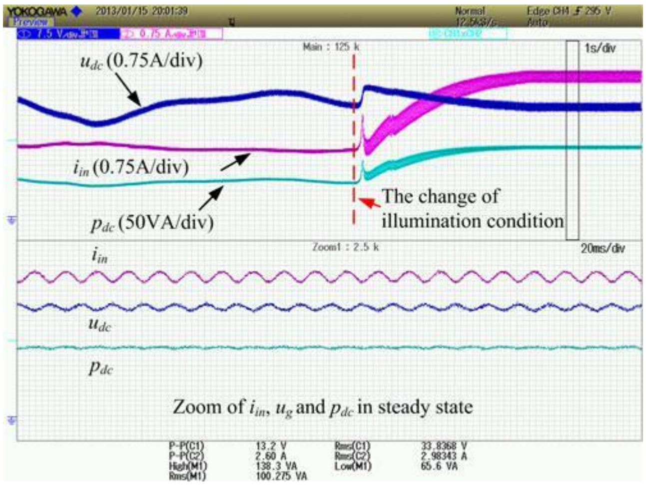

Fig. 39. Voltage, current and power of PV panel.

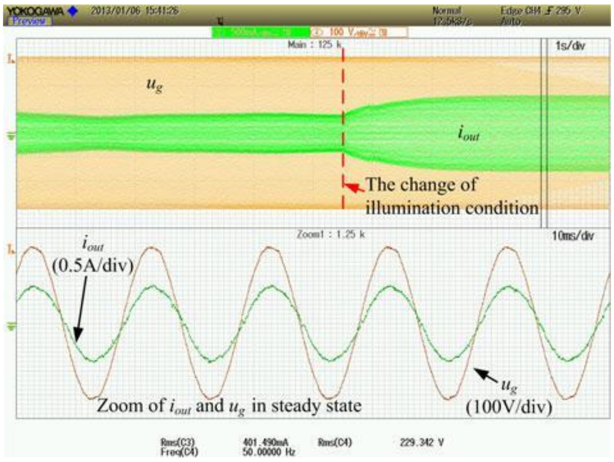

Fig. 40. Output current of ACM and grid voltage.

The MPPT control strategy is based on the proposed method in Section V.

Figs. 39 and 40 illustrate the dynamic response of the ACM when the illumination condition changes form partial occlusion to no occlusion. In these figures, the changing of illumination condition happened at the instant of the dash line.

Fig. 39 shows the voltage u_{dc} and current i_{in} of the PV panel. In this figure, the product of u_{dc} and i_{in} , which is the instanta-neous power p_{dc} of PV panel. Fig. 40 shows the output current $i_{out}$of ACM and the grid voltage u_g. The dynamic responselasts for about 2 seconds. Finally, the output power is stabilized around 138 W according to Fig. 39, which is close to the max-imum power point of the PV panel. Thus, the proposed MPPT control method is implemented by changing I_A is validated.

VIII. CONCLUSION

Flyback inverter is an attractive solution for photovoltaic ac module application. As a grid-connected device, flyback inverter should work as a current source and provides the sinusoidal output current that is synchronous with the grid voltage. Mean- while, the flyback inverter should have high efficiency to satisfy user's demand.

In this topology, BCM is more preferred compared to DCM and CCM, because of its higher power level, higher efficiency, and wider switching frequency bandwidth. However, the control of BCM is more complicated, due to its VSF. This also leads to the difficulty to get the accurate mathematical model between output current i_{out} and reference current i_{ref} , which has a great influence on THD of i_{out} .

In this paper, the relationship between ACM output current $i_{out}$and reference current $i_{ref}$of flyback inverter in BCM isinvestigated, and an accurate mathematical model is proposed through theoretical derivation. Then, a novel control strategy of $i_{ref}$is proposed to decrease THD of i_{out}. Moreover, the real-ization of MPPT based on this control strategy is also investi-gated. Finally, simulation and experiment results of an improved flyback-inverter topology are presented, which verifies the pro-posed control strategy.

ACKNOWLEDGMENT

The authors would like to thank Altenergy Power System Inc. of China, for the support of PV ACM power stage during the project. The authors would also like to thank PLEXIM Inc., for the support of the powerful system-level simulation tool PLECS.

REFERENCES

[1] W. Bower, R. West, and A. Dickerson, "Innovative PV micro-inverter topology eliminates electrolytic capacitors for longer lifetime," in *Proc.Conf. Rec. 2006 IEEE 4th World Conf. Photovoltaic Energy Convers.,*vol. 2, May 7–12, 2006, pp. 2038–2041.

[2] J. J. Bzura, "The AC module: An overview and update on self-contained modular PV systems," in *Proc. 2010 IEEE Power Energy Soc. GeneralMeeting*, Jul. 25–29, 2010, pp. 1–3.

[3] R. H. Wills, S. Krauthamer, A. Bulawka, and J. P. Posbic, "The AC photo-voltaic module concept," in *Proc. Proc. 32nd Intersociety Energy Convers.Eng. Conf. (IECEC-97)*, 27 Jul.–1 Aug., 1997, vol. 3, pp. 1562–1563.

[4] E. Roman,´ R. Alonso, P. Ibanez,˜ S. Elorduizapatarietxe, and D. Goitia, "Intelligent PV module for grid-connected PV systems," *IEEE Trans. Ind.Electron.*, vol. 53, no. 4, pp. 1066–1073, Jun. 2006.

[5] B. Liu, S. Duan, and T. Cai, "Photovoltaic DC-building-module-based BIPV system—Concept and design considerations," *IEEE Trans. PowerElectron.*, vol. 26, no. 5, pp. 1418–1429, May 2011.

[6] S. B. Kjaer, J. K. Pedersen, and F. Blaabjerg, "A review of single-phase grid-connected inverters for photovoltaic modules," *IEEE Trans. Ind.Appl.*, vol. 41, no. 5, pp. 1292–1306, Sep./Oct. 2005.

[7] W. Yu, C. Hutchens, J.-S. Lai, J. Zhang, G. Lisi, A. Djabbari, G. Smith, and T. Hegarty, "High efficiency converter with charge pump and coupled inductor for wide input photovoltaic AC module applications," in *Proc.Energy Convers. Congr. Expo.*, Sep. 20–24, 2009, pp. 3895–3900.

[8] X. Yuan and Y. Zhang, "Status and opportunities of photovoltaic inverters in grid-tied and micro-grid systems," in *Proc. CES/IEEE 5th Int. PowerElectron. Motion Control Conf. (IPEMC 2006)*, Aug. 14–16, 2006, vol. 1,pp. 1–4.

[9] S. V. Araujo,´ P. Zacharias, and R. Mallwitz, "Highly efficient single-phase transformerless inverters for grid-connected photovoltaic systems," *IEEETrans. Ind. Electron.*, vol. 57, no. 9, pp. 3118–3128, Sep. 2010.

[10] B. Sahan, A. N. Vergara, N. Henze, A. Engler, and P. Zacharias, "A single-stage PV module integrated converter based on a low-power current-source inverter," *IEEE Trans. Ind. Electron.*, vol. 55, no. 7, pp. 2602–2609, Jul. 2008.

[11] N. Papanikolaou, E. Tatakis, A. Ciritsis, and D. Klimis, "Simplified high frequency converters in decentralized grid-connected PV systems: A novel low-cost solution," in *Proc. 9th Eur. Conf. Power Electron. Appl.(EPE'2003)*, Toulouse, France, Jun. 15–19, 2003, paper on CD.

[12] A. C. Nanakos, E. C. Tatakis, and N. P. Papanikolaou, "A weighted-efficiency-oriented design methodology of flyback inverter for AC photo-voltaic modules," *IEEE Trans. Power Electron.*, vol. 27, no. 7, pp. 3221– 3233, Jul. 2012.

[13] T. Shimizu, K. Wada, and N. Nakamura, "A flyback-type single phase utility interactive inverter with low-frequency ripple current reduction on the DC input for an AC photovoltaic module system," in *Proc. 2002IEEE 33rd Annu. Power Electron. Spec. Conf. (PESC'02)*, 2002, vol. 3,
pp. 1483–1488.

[14] S. B. Kjaer and F. Blaabjerg, "Design optimization of a single phase inverter for photovoltaic applications," in *Proc. 2003 IEEE 34th Annu.Power Electron. Spec. Conf. (PESC'03)*, Jun. 15–19, 2003, vol. 3,
pp. 1183–1190.

[15] Y. Li and R. Oruganti, "A low cost flyback CCM inverter for AC module application," *IEEE Trans. Power Electron.*, vol. 27, no. 3, pp. 1295–1303, Mar. 2012.

[16] Y. Li and R. Oruganti, "A flyback-CCM inverter scheme for photovoltaic AC module application," in *Proc. Power Eng. Conf. (AUPEC'08)*, Dec. 14–17, 2008, pp. 1–6.

[17] A. Ch. Kyritsis, E. C. Tatakis, and N. P. Papanikolaou, "Optimum design of the current-source flyback inverter for decentralized grid-connected photovoltaic systems," *IEEE Trans. Energy Convers.*, vol. 23, no. 1, pp 281–293, Mar. 2008.

[18] Y.-H. Ji, D.-Y. Jung, J.-H. Kim, C.-Y. Won, and D.-S. Oh, "Dual mode switching strategy of flyback inverter for photovoltaic AC modules," in *Proc. 2010 Int. Power Electron. Conf. (IPEC)*, Jun. 21–24, 2010, pp. 2924–2929.

[19] A. Kyritsis, N. Papanikolaou, E. Tatakis, and J. Kobougias, "Design and control of a current source flyback inverter for decentralized grid-connected photovoltaic systems," in *Proc. 2005 Eur. Conf. Power Elec-tron. Appl.*, Jun. 15–19, 2005, pp. 1–10.

[20] Z. Zhang, M. Chen, M. Gao, Q. Mo, and Z. Qian, "An optimal control method for grid-connected photovoltaic micro-inverter to improve the efficiency at light-load condition," in *Proc. 2011 IEEE Energy Convers.Congr. Expo. (ECCE)*, Sep. 17–22, 2011, pp. 219–224.

[21] Z. Zhang, C. Zhang, M. Chen, and Z. Qian, "An improved on-time control method to reduce the line-current distortion for BCM-DCM mixed micro-inverter at light load condition," in *Proc. 2012 IEEE Int. Symp. Ind.Electron. (ISIE)*,, May 28–30, 2012, pp. 1760–1764.

[22] T. Shimizu, K. Wada, and N. Nakamura, "Flyback-type single-phase utility interactive inverter with power pulsation decoupling on the DC input for an AC photovoltaic module system," *IEEE Trans. Power Electron.*, vol. 21, no. 5, pp. 1264–1272, Sep. 2006.

[23] G. H. Tan, J. Z. Wang, and Y. C. Ji, "Soft-switching flyback inverter with enhanced power decoupling for photovoltaic applications," *Electric PowerAppl., IET*, vol. 1, no. 2, pp. 264–274, Mar. 2007.

[24] H. Hu, S. Harb, X. Fang, D. Zhang, Q. Zhang, Z. J. Shen, and I. Batarseh, "A three-port flyback for PV microinverter applications with power pulsa-tion decoupling capability," *IEEE Trans. Power Electron.*, vol. 27, no. 9, pp 3953–3964, Sep. 2012.

[25] T. Hirao, T. Shimizu, M. Ishikawa, and K. Yasui, "A modified modulation control of a single-phase inverter with enhanced power decoupling for a photovoltaic AC module," in *Proc. 2005 Eur. Conf. Power Electron. Appl.*, Jun. 15–19, 2005, pp. 1–10.

[26] N. Kasa, T. Iida, and A. K. S. Bhat, "Zero-voltage transition flyback in-verter for small scale photovoltaic power system," in *Proc. IEEE 36thPower Electron. Spec. Conf. (PESC'05)*, Jun. 16, 2005, pp. 2098–2103.

[27] J.-Y. Gu, H.-F. Wu, G.-C. Chen, and Y. Xing, "Research on photovoltaic grid-connected inverter based on soft-switching interleaved flyback con-verter," in *Proc. 2010 5th IEEE Conf. Ind. Electron. Appl. (ICIEA)*, Jun. 15–17, 2010, pp. 1209–1214.

[28] Q. Mo, M. Chen, Z. Zhang, M. Gao, and Z. Qian, "Research on a non-complementary active clamp flyback converter with unfolding DC–AC inverter for decentralized grid-connected PV systems," in *Proc. 2011 IEEEEnergy Convers. Congr. Expo. (ECCE)*, Sep. 17–22, 2011, pp. 2481–2487.

[29] N. Kasa, T. Iida, and L. Chen, "Flyback inverter controlled by sensorless current MPPT for photovoltaic power system," *IEEE Trans. Ind. Electron.*, vol. 52, no. 4, pp. 1145–1152, Aug. 2005.

[30] Y.-H. Kim, J.-G. Kim, Y.-H. Ji, C.-Y. Won, and T.-W. Lee, "Flyback inverter using voltage sensorless MPPT for AC module systems," in *Proc.2010 Int. Power Electron. Conf. (IPEC)*, Jun. 21–24, 2010, pp. 948–953.

[31] S. J. Chiang, K. T. Chang, and C. Y. Yen, "Residential photovoltaic energy storage system," *IEEE Trans. Ind. Electron.*, vol. 45, no. 3, pp. 385–394, Jun. 1998.

[32] B. K. Bose, P. M. Szczesny, and R. L. Steigerwald, "Microcomputer con-trol of a residential photovoltaic power conditioning system," *IEEE Trans.Ind. Appl.*, vol. IA-21, no. 5, pp. 1182–1191, Sep. 1985.

[33] J.-S. Lai, "Power conditioning systems for renewable energies," in *Proc.Int. Conf. Electr. Machines Syst. (ICEMS)*, Oct. 8–11, 2007, pp. 209–218.

[34] Z. Zhang, X.-F. He, and Y.-F. Liu, “An optimal control method for photo-voltaic grid-tied interleaved flyback micro-inverters to achieve high effi-ciency in wide load range,” *IEEE Trans. Power Electron.*, vol. 28, no. 11, pp 5074–5087, Nov. 2013.

[35] R. W. Erickson and D. Maksimovic, *Fundamentals of Power Electronics*. Norwell, MA, USA: Kluwer, 1997.

[36] W. Xiao and W. G. Dunford, “A modified adaptive hill climbing MPPT method for photovoltaic power systems,” in *Proc. 2004 IEEE 35thAnnu. Power Electron. Spec. Conf. (PESC’04)*, Jun. 20–25, 2004, vol. 3, pp 1957–1963.

[37] K. H. Hussein, I. Muta, T. Hoshino, and M. Osakada, “Maximum pho-tovoltaic power tracking: An algorithm for rapidly changing atmospheric conditions,” *IEE Proc. Generation, Transmiss. Distrib.*, vol. 142, no. 1, pp 59–64, Jan. 1995.

[38] F. Liu, S. Duan, F. Liu, B. Liu, and Y. Kang, “A variable step size INC MPPT method for PV systems,” *IEEE Trans. Ind. Electron.*, vol. 55, no. 7, pp 2622–2628, Jul. 2008.

[39] Y.-C. Kuo, T.-J. Liang, and J.-F. Chen, “Novel maximum-power-point-tracking controller for photovoltaic energy conversion system,” *IEEETrans. Ind. Electron.*, vol. 48, no. 3, pp. 594–601, Jun. 2001.

[40] A. Durgadevi, S. Arulselvi, and S. P. Natarajan, “Study and implementa-tion of maximum power point tracking (MPPT) algorithm for Photovoltaic systems,” in *Proc. 2011 1st Int. Conf. Electr. Energy Syst. (ICEES)*, Jan. 3–5, 2011, pp. 240–245.

[41] *Characteristics of the Utility Interface for Photovoltaic (PV) Systems*, IEC61727 CDV, 2002.

[42] *IEEE Standard for Interconnecting Distributed Resources with Electric Power Systems*, IEEE Std. 1547, 2003.

N UdayaSankara Reddy (M’93) was born in Chittoor, JangalaPalli, in 1993. He received the **B.E in Electrical & Electronics engineering** from JNTUA University, Anantapur, in 2010 and 2014, re-spectively.